Design and tuning electronic structure of nickel-vanadium layered double hydroxide for highly efficient oxygen evolution reaction

Harish S. Chavan,[a+] Chi Ho Lee,[b+] Akbar I. Inamdar,*[a] Yongcheol Jo,[a,c] Sang Uck Lee,[b]* Bo Hou,[d,δ] Hyunsik Im,*[a] Hyungsang Kim*[a]

[a]Division of Physics and Semiconductor Science, Dongguk University, Seoul 04620, South Korea

[b]Department of Applied Chemistry, Center for Bionano Intelligence Education and Research, Hanyang University ERICA, Ansan 15588, South Korea

[c]Quantum-functional Research Centre, Dongguk University, Seoul 04620, South Korea

[d]Department of Engineering Science, University of Oxford, Parks Road, OX1 3PJ, UK

*Corresponding Authors

*E–mail: akbarphysics2002@gmail.com, hyunsik7@dongguk.edu, hskim@dongguk.edu, sulee@hanyang.ac.kr

+ H. S. Chavan and C. H. Lee contributed equally to this work.

$^{\delta}$ Present address: School of Physics and Astronomy, Cardiff University, Cardiff, CF24 3AA, Wales, UK.

ABSTRACT

Obtaining deep insight into the relationship between the optimal composition and high oxygen-evolving ability of multi-metal layered double hydroxides (LDHs) at the microscopic level is of great importance. Herein, we report experimental and density functional theory (DFT) investigations into the oxygen evolution reaction (OER) of nickel (Ni)-vanadium (V) LDHs to obtain an optimal electrocatalyst via changing the composition ratio. The DFT calculations elucidate that catalytically active oxygen (O) binding sites play an essential role in facilitating the initiation of the OER process, thereby leading to enhanced conductivity due to their significant contribution to the bands around

the Fermi level. The optimized $Ni_{0.75}V_{0.25}$ LDH has not only a lower hydrogen desorption energy but also the most open O sites, thereby promoting initiation of the OER reaction. OER performance evaluation of Ni-V LDHs reveals that the $Ni_{0.75}V_{0.25}$ LDH electrocatalyst shows the best OER properties, which is consistent with the theoretical prediction.

Keywords: electrocatalysis, water splitting, oxygen evolution reaction, $Ni_{1-x}V_x$ LDH, energy generation

1. Introduction

Hydrogen is the most abundant element on Earth and an ideal energy source that could substitute for conventional fossil fuels to sustain the rapid increase in energy consumption required in everyday life [1-3]. Harvesting clean hydrogen and oxygen gases for use as energy sources in fuel cells and rechargeable metal-air batteries via electrochemically splitting water has attracted considerable attention because it has become economically viable and is environment-friendly [4-6]. Electrochemical water splitting is based on two different electrocatalytic reactions: the hydrogen evolution reaction (HER) and the oxygen evolution reaction (OER). Especially, the OER half-reaction using novel anode materials has been more intensively investigated due to its sluggish reaction kinetics [7-9]. In practical water splitting systems, unavoidable competing side reactions occur resulting in reduced ideal Faradaic efficiency. Thus, electrocatalysis in water electrolysis requires excess energy in the form of overpotential to overcome the various activation barriers. The theoretical potential required to split water into hydrogen and oxygen gases is 1.23 V [10]. Even though precious inert metals such as platinum (Pt), iridium (Ir), and ruthenium (Ru) and their alloys are commonly used in electrocatalysis, there are considerable challenges, such as their high cost and relative scarcity, when using them in large-scale applications [11-13].

Recently, a tremendous amount of research has been carried out on fabricating efficient OER catalysts using layered double hydroxides (LDHs) of nickel (Ni), iron (Fe), and cobalt (Co), and their complex compounds [14-24]. A survey of the available literature on the current status of electrochemical water splitting technology for OER based on transition metal oxides and hybrid transition metal complexes, along with our work, is presented in **Fig. 1 (a).** From the literature review, it seems obvious that LDHs have outstanding oxygen-evolving characteristics due to their large specific surface area, unique layered structure, tunable elemental composition, etc. Especially, the incorporation of Fe or Co into the matrix of nickel (II) oxide (NiO)/hydroxide ($Ni(OH)_2$) is one of the most popular routes for achieving high catalytic performance. The idea behind multi-metal LDHs is to enhance the number of active sites and intrinsic catalytic activity by varying the relative ratio of the constituent metals. However, based on the literature survey, searching for earth-abundant materials based LDHs with excellent activity for water electrolysis superior to that of Ni-Fe LDH is still challenging.

Density functional theory (DFT) calculations enable the practical design of complex catalytic materials, including multi-metal hydroxides, via a comprehensive understanding of the mechanism of water oxidation at the atomic level as well as key performance factors.[30-33] Although significant efforts and advances have been made to elucidate the high OER activity of state-of-the-art multi-metal oxides and hydroxides, particularly in the calculation of the electronic structures and electrocatalytic mechanism, comparing the theoretical effects of the composition of the constituent metals on the oxygen-evolving activity with experimental data has not been rigorously carried out. Furthermore, as the metal composition changes, the active site structure also varies, leading to significant uncertainty in the relationship between the active site structure and the catalytic mechanism. Therefore, it is of great importance to theoretically explore this relationship to predict the optimal performance of new catalysts.

In this work, we present comprehensive research on the synthesis, electrochemical properties and oxygen evolution reaction of Ni-vanadium (V) LDH electrocatalysts, elucidating

the correlation between OER performance and Ni/V compositional ratio through state-of-the-art DFT calculations and electrochemical analysis. A series of $Ni_{1-x}V_x$ LDH ($0 \leq x \leq 1$) electrocatalysts were fabricated on stainless-steel substrates via chemical bath deposition (CBD). **Fig. 1 (b)** shows a schematic of the CBD method and the evolution of the surface morphology of the $Ni_{1-x}V_x$ LDH films with increasing V content. The best optimized $Ni_{0.75}V_{0.25}$ LDH catalyst attained a very low overpotential of 200 mV for OER at 10 mA cm^{-2} and exhibited outstanding stability for more than 100 hours, while the obtained low Tafel slope of 48.1 $mVdec^{-1}$ indicates a faster mass and electron transfer rate at the catalyst/electrolyte interface than those of other LDHs. Moreover, according to the DFT calculations, the enhanced catalytic activity of the best $Ni_{0.75}V_{0.25}$-LDH can be attributed to the existence of the highest number of active O_{VNN} sites (where subscripts N and V represent nickel and vanadium respectively), lowest hydrogen desorption energy (HDE), and enhanced conductivity.

2. Experimental Section

2.1. Preparation of $Ni(OH)_2$ and $Ni_{1-x}V_x$ LDH thin films

A CBD method was used to synthesize the LDH thin films on stainless-steel substrates. Supplementary Information **Fig. 1(b)** provides a schematic representation of the CBD technique employed for $Ni_{1-x}V_x$ LDH synthesis. Precursor chemicals nickel chloride ($NiCl_2 \cdot 6H_2O$), sodium orthovanadate (Na_3VO_4), and ammonia solution were purchased from Sigma-Aldrich and used without further purification. Different molar ratios of Ni to V (0.95:0.05, 0.90:0.10, 0.80:0.20, 0.75:0.25, 0.50:0.50, and 0.25:0.75) were used. For comparison, pure $Ni(OH)_2$ and vanadium hydroxide ($V(OH)_2$) were synthesized using 1:0 and 0:1 molar ratios, respectively. Precursor solutions were prepared in 60 ml of distilled water. Afterwards, 10 ml of ammonia solution was added to adjust the pH value to 11.4. The mixture solution was transferred to a glass beaker and heated at 80 □C for 10 h while continuously

stirring using a magnetic stirring bar during the deposition. After the deposition, the films were rinsed with distilled water and dried under N_2 gas.

2.2. Material characterization

XRD patterns of the films were recorded using an X-ray diffractometer with Ni-filtered Cu–Kα radiation (Ka α–1.54056 Å) (X pert PRO, Panalytical, Netherlands). Raman spectra were recorded with a LabRam Armis (Horiba Jobin Yvon, USA) with an Ar–ion laser beam (λ = 514.5 nm). The surface morphology was observed using field emission SEM (JSM–6701F, JEOL, Japan). The chemical states of the films were investigated using XPS (Versaprobe II, Ulvac–phi, Inc., Japan). The microscopic structural properties of the samples were investigated using TEM, HAADF-STEM with an Oxford EDX detector (Oxford Instruments Plc., UK), HR–TEM, and SAED on a JEOL 3000F (JEOL, Japan) at 300 kV.

2.3. Electrochemical measurements

These were carried out using the three-electrode configuration consisting of a working electrode ($Ni_{1-x}V_x$ LDHs), a counter electrode (Pt wire), and a reference electrode (saturated calomel electrode, SCE). 1 M KOH electrolyte was used in all of the electrochemical experiments. The applied potential was converted to potential with respect to the reversible hydrogen electrode (RHE) using the standard conversion formula. The electrochemical measurements were carried out using a Versa–stat–3 electrochemical workstation (Princeton Applied Research, USA). The electrodes were initially cycled using a CV technique until a stable potential was observed. After the LSV had been measured in a potential window of 0 to 0.7 versus SCE at a scan rate of 5 mV/s, the stability of the electrode was measured using chronopotentiometry at a fixed current density (j) of 10 mA cm^{-2}. The ECSAs of the electrodes

were estimated from their CV curves measured at different scan rates of 10, 20, 30, 40, and 50 mVs^{-1}. The Tafel slopes were determined using plots of overpotential (η) against log (*j*).

3. Results and discussion

3.1. DFT calculations and theoretical model

We propose a theoretical guideline for developing highly active OER electrocatalysts by incorporating transition metals (TMs) into the Ni-TM LDH structure (**Fig. 2a**). To rationally design $Ni_{1-x}TM_x$ LDH ($0 \leq x \leq 1$) structures and investigate their OER catalytic activities, we preferentially constructed a series of $Ni_{1-x}Fe_x$ LDHs ($0 \leq x \leq 1$) by systematically varying the Ni/Fe ratio and investigated the optimal structure for each combination of the ratio (Supplementary Information **Fig. S1**). Next, we evaluated their hydrogen desorption energy **(**HDE) values because it is an essential indicator in judging the initiation of the OER process in the LDH system. Even though there is still controversy about whether TM or oxygen (O) comprises the OER active sites, it is undisputed that oxide binding to the TM sites is not desirable due to severe steric hindrance, especially in the basal plane. Hence, we reasonably considered the O sites to be the OER active sites and systematically explored HDE values of all possible O binding sites (O_{NNN}, O_{FNN}, O_{FFN}, and O_{FFF}, where subscripts N = Ni and F = Fe) to ascertain favorable open O sites for oxide binding. The calculated HDE values in **Fig. S2** (Supplementary Information) reveal that the $Ni_{0.75}Fe_{0.25}$ LDH structure has the lowest HDE value except for that of $Fe(OH)_2$, which is structurally unstable due to severe hydrogen (H) shedding [25,26]. Furthermore, only this atomic configuration can lead to well-dispersed V atoms that efficiently reduce the number of O_{NNN} sites while maintaining the highest HDE (Supplementary Information **Fig. S2**). From these observations, one can envisage that the $Ni_{0.75}Fe_{0.25}$ LDH structure would be more catalytically active because the active formation of open O sites plays a vital role in facilitating the initiation of the OER process. Based on this

theoretical evaluation, we then constructed all possible TM-incorporated LDH structures ($Ni_{0.75}TM_{0.25}$ LDHs) using the confirmed $Ni_{0.75}Fe_{0.25}$ LDH structure with dispersed Fe atoms.

From the $Ni_{0.75}TM_{0.25}$ LDH structures designed using each of the 28 TMs, we attempted to evaluate the OER overpotential (η^{OER}) values for all possible open O active sites based on the two-step reaction pathway associated with the O* intermediate [27,28] (detailed derivation of the free energy relationship is described in the Supplementary Information). Using the calculated reaction Gibbs free energy values of the O binding sites (ΔG_{O*}), we created an OER volcano plot (**Fig. 2b**) that represents the apparent activity correlation between $-\eta^{OER}$ and ΔG_{O*} and found that there are many attractive OER catalyst candidates with remarkably low η^{OER}. Above all, the $Ni_{0.75}V_{0.25}$ LDH with dispersed V atoms has the lowest η^{OER} of 0.23 V, which indicates that it has much better catalytic performance than that of conventional ruthenium (IV) oxide (RuO_2; 0.42 V). To verify the reliability of the remarkable catalytic activity of the specific $Ni_{0.75}V_{0.25}$ LDH composition, we additionally conducted comparative studies for all possible compositions of $Ni_{1-x}V_x$ LDHs ($0 \leq x \leq 1$). According to our calculations, interpretation of the constructed free energy diagrams (FEDs) and the volcano plot led us to infer that the $Ni_{0.75}V_{0.25}$ LDH is still the best structure and exhibits exceptional OER performance because it has the optimal ΔG_{O*} (**Fig. 2c** and Supplementary Information **Fig. S3)**. These findings also validate the reliability of our proposed approach when screening the OER activities of the TM-doped LDH system.

To understand the dependence of OER activities on the V-incorporated Ni-based LDH structures, we explored their geometric and electronic features because these play crucial roles in enhancing inherent OER activity (**Figs. 2d–f** and Supplementary Information **Figs. S4–S7**). When considering the geometric effect, one expects that different V doping ratios will lead to various local structural environments in the $Ni_{1-x}V_x$ LDHs due to different arrangements of the V dopant. Therefore, the O active sites can be classified into O_{NNN}, O_{VNN}, O_{VVN}, and O_{VVV} sites (**Supplementary Information Fig. S4**), depending on the TM environment. This allows us to

clearly understand how the environment around the O sites affects the OER catalytic activity. Based on this structural viewpoint, we systematically investigated the HDE values according to the different O sites mentioned above (Supplementary Information **Fig. S5**); it is noteworthy that the O_{VNN} site is the most energetically favorable. Moreover, the $Ni_{0.75}V_{0.25}$ LDH has not only the lowest HDE value but also the highest O_{VNN} ratio (**Fig. 2d**). Hence, we can assert that $Ni_{0.75}V_{0.25}$ LDH has the most open O sites which help to facilitate the initiation of the OER process better than in the other Ni-V LDH structures.

To obtain insight into the difference in H desorption between the different O sites, we analyzed their *p*-band centers using the partial density of states (PDOS) because H binding strength is generally evaluated through the *p*-level of the O site that hybridizes with the H atoms state. Analysis results of *p*-band centers, shown in **Fig. 2e** and **Supplementary Information Fig. S6**, reveal that the O_{VNN} site has the lowest value based on the following order: O_{VNN} (−6.7 eV) < O_{VVN} (−5.8 eV) < O_{VVV} (−5.1 eV) < O_{NNN} (−2.9 eV). This result implies that the lower-lying *p*-level can lead to an inactive chemical bond by ineffectively hybridizing with the H atomic state, so that the O_{VNN} site yields the most favorable H desorption with the improved OER initial reaction. Next, we paid attention to changes in the total O charge attributed to V atoms in $Ni_{0.75}V_{0.25}$ LDH through a comparison with $Ni_{1.0}$ LDH, because the catalytic activity can be significantly affected by variation of electron concentration on active sites. Interestingly, the results shown in Supplementary Information **Fig. S7** indicate efficient electron transfer from V to O atoms, and this accepting of electrons results in a metallic property by shifting the band structure down via *n*-type doping effect.

To obtain deeper understanding of the electronic structure, we decomposed the elemental band structures of $Ni_{1-x}V_x$ LDHs (x = 0 and 0.25) and focused on the O active sites (**Fig. 2f**) because the activity improvement is strongly correlated with the contribution of the active sites to the frontier bands around the Fermi level [29]. The analysis results indicate, unusually, that O sites in $Ni_{0.75}V_{0.25}$ LDH predominantly contribute to the bands around the

Fermi level, while they contribute to bands below the Fermi level in $Ni_{1.0}$ LDH. Besides this, when considering the compositional abundance of O sites in the LDH system, $Ni_{0.75}V_{0.25}$ LDH shows enhanced conductivity because the O sites significantly contribute to the bands around the Fermi level. In particular, it should be noted that $Ni_{0.75}V_{0.25}$ LDH has a substantial O_{VNN} ratio (see **Fig. 2d**), so that most of the active sites are located at the Fermi level, which can effectively boost the OER. These theoretical insights reveal that the O_{VNN} site plays an essential role in facilitating the initial OER process and, strikingly, that $Ni_{0.75}V_{0.25}$ LDH exhibits superior OER performance in alkaline media due to synergy between its geometry and the electronic activity.

3.2. Structural analysis and morphological characterization of $Ni_{1-x}V_x$ LDHs

Figure 3a shows X-ray diffraction (XRD) spectra of the $Ni_{1-x}V_x$ LDH electrocatalysts, in which systematic evolution of the XRD patterns can be observed upon V incorporation into the $Ni(OH)_2$ matrix. First, the XRD spectrum of pure $Ni(OH)_2$ matches well with that of β-$Ni(OH)_2$ phase (JCPDS 14-0117) [30], with corresponding (001), (100), (101), (102), (110), (111), and (202) reflection planes exhibiting a layered structure. Moreover, the diffraction peak intensities are reduced by incorporating V into the $Ni(OH)_2$ matrix. A characteristic feature upon V incorporation into the $Ni(OH)_2$ matrix is the appearance of a low intense broad peak around 34.23° in the XRD spectrum of $Ni_{0.8}V_{0.2}$ and $Ni_{0.75}V_{0.25}$ LDHs, which corresponds to the characteristic (009) facet of NiV LDH (PDF 52-1627), revealing that $Ni_{0.8}V_{0.2}$ and $Ni_{0.75}V_{0.25}$ LDHs are isomorphous, like layered β-$Ni(OH)_2$. On the other hand, the pure vanadium (II) hydroxide $V(OH)_2$ film is amorphous. It is clear that the incorporation of V into the $Ni(OH)_2$ matrix deteriorates the crystallinity due to strain-induced lattice distortion and reduction in crystal symmetry [31].

The chemical bonding state of the NiV LDH films was examined via Raman spectroscopy (**Fig. 3b**). The peaks observed at 314 and 449.8 cm^{-1} in the spectrum for pure $Ni(OH)_2$ are attributed to Raman–active vibrations of the E_g and A_{1g} modes of β–$Ni(OH)_2$, respectively [32]. As V is incorporated into the $Ni(OH)_2$ matrix, the Raman spectrum changes dramatically, showing a reduction in intensity of the E_g and A_{1g} modes. The feature of multiple broad peaks of $Ni_{1-x}V_x$ LDHs ranging between 700 and 900 cm^{-1} is due to the second-order lattice mode of $Ni(OH)_2$ and the symmetric-stretching vibrational modes of the $[V_2O_7]^{4-}$ and $[V_4O_{12}]^{4-}$[32]. The systematic shift in peak position and the peak broadening are clear indicators of the incorporation of V into the $Ni(OH)_2$ matrix which causes lattice distortion and reduction in crystal symmetry. The Raman spectrum of pure $V(OH)_2$ shows peaks in the range of 700–1100 cm^{-1}, which are mainly due to stretching modes of the $(VO_4)^{3-}$ tetrahedron [33,34].

Microstructural and structural analysis of the $Ni(OH)_2$ and $Ni_{1-x}V_x$ LDH catalyst films were performed using scanning electron microscopy (SEM) and transmission electron microscopy (TEM) techniques; SEM, TEM, high-resolution TEM (HRTEM), selected area electron diffraction (SAED), and high-angle annular dark field-scanning transmission electron microscopy (HAADF-STEM) images of the $Ni(OH)_2$ electrocatalyst are provided and discussed in detail in Supplementary Information **Fig. S8**. As V atoms are incorporated into the $Ni(OH)_2$ matrix, the surface morphology changes dramatically (Supplementary Information **Fig. S9a–f**). The compositional Ni/V ratio plays a critical role in determining the morphology of the $Ni_{1-x}V_x$ LDHs because the incorporation of V atoms changes the growth kinetics. Vanadium (50.94 amu), having a lower atomic weight in the precursor solution, affects the reaction rate and leads to the different surface morphologies. The atomic molar ratios determined from the energy-dispersive X-ray spectroscopy (EDX) analysis are close to those used in the precursor solution for the $Ni_{1-x}V_x$ LDHs with $x \leq 0.5$ (Supplementary Information **Table S1** and **Figs. S10** and **S11**).

Figures 3c and 3d show SEM and TEM images of the $Ni_{0.75}V_{0.25}$ LDH film, respectively, which clearly exhibits a thin silk-like morphology. The HRTEM image in **Fig. 3e** reveals the lattice fringes of the $Ni_{0.75}V_{0.25}$ LDH sample with lattice spacings of 0.22 and 0.26 nm, which correspond to the (015) and (101) planes of NiV LDH (JCPDS-38-0715), respectively [30]. The measured SAED pattern in **Fig. 3f** shows broad diffuse rings, which indicate that the film is a combination of amorphous and polycrystalline structures [35]. The HAADF-STEM and EDX mapping images of $Ni_{0.75}V_{0.25}$ LDH in **Fig. 3g–j** reveal that the constituent elements Ni, V, and O are uniformly distributed over the sample. STEM elemental line scans in Supplementary Information **Fig. S12a-d** also demonstrate the uniform distribution of Ni, V, and O even at micrometer length scales.

3.3 Chemical valance states

The evolution of the chemical and electronic states of the constituent elements in the $Ni(OH)_2$ and $Ni_{1-x}V_x$ LDH films was investigated using X-ray photoelectron spectroscopy (XPS) measurements. **Figure 4** shows the XPS spectra of the $Ni(OH)_2$ and $Ni_{0.75}V_{0.25}$ LDH samples. The XPS survey spectra in **Fig. 4a** reveal the presence of Ni, V, and O in the films. Meanwhile, the core-level Ni 2*p* spectra in **Fig. 4b** show main peaks at 855.87 eV and 873.62 eV, along with their satellite peaks, which are associated with the Ni^{2+} binding states of Ni $2p_{3/2}$ and Ni $2p_{1/2}$, respectively. The binding energy difference between these two peaks is 17.75 eV, revealing the formation of Ni^{2+} oxidation states [36,37]. For the $Ni_{0.75}V_{0.25}$ LDH film, the Ni $2p_{3/2}$ and Ni $2p_{1/2}$ peaks shift slightly toward the lower binding energy side (indicated with dotted lines) due to the electronic interaction between Ni to V and interfacial charge transfer upon V doping [38]. Furthermore, the V 2*p* spectrum of the $Ni_{0.75}V_{0.25}$ LDH film (see Supplementary Information **Fig. S13 and Fig. 4c**) exhibits two peaks at 516.5 and 524 eV, which are associated with V $2p_{3/2}$ and V$3p_{1/2}$, respectively; their binding energy difference is 7.5 eV, which can be attributed to spin-orbit splitting [39]. The deconvoluted V $2p_{3/2}$ spectrum

in **Fig. 4c** consists of two peaks at 516.51 (purple) and 517.95 eV (green), associated with the V^{4+} and V^{5+} oxidation states, respectively[4], and these higher oxidation states are catalytically active [40]. The deconvoluted peaks at 529.3, 530.5, 531.9, and 533.15 eV in the O 1*s* spectrum (**Fig. 4d**) are linked with VO_2, $Ni(OH)_2$, nickel oxyhydroxide (NiOOH), and H_2O, respectively.

3.4. OER electrocatalytic performance

The electrocatalytic activities of the $Ni_{1-x}V_x$ LDH ($0 \leq x \leq 1$) electrodes were measured by linear sweep voltammetry (LSV) in a 1 M KOH electrolyte at a scan rate of 5 mVs^{-1}. Prior to the LSV, the catalyst films were activated by carrying out cyclic voltammetry (CV) measurements for 1000 cycles, after which the electrocatalytic water oxidation parameters were measured. Details about the initial activation of the electrocatalyst are provided in Supplementary Information **Fig. S14 a–c**. Full-scale LSV curves of the catalysts are shown in **Fig. 5a**, and their enlarged LSV curves at a current density of 10 mA cm^{-2} are shown in **Fig. 5b**. For comparison, the LSV curves of the $Ni(OH)_2$ and $V(OH)_2$ films are also presented. The measured LSV curves clearly demonstrate that the incorporation of V in the $Ni(OH)_2$ matrix plays an important role in determining the catalytic activity of the $Ni_{1-x}V_x$ LDHs. The $Ni_{0.75}V_{0.25}$ LDH catalyst exhibits an excellent oxygen-evolving reaction with the lowest overpotential of 200 mV at 10 mA cm^{-2} (292 mV at 400 mA cm^{-2}). Furthermore, the OER electrocatalytic reaction kinetics were evaluated by measuring the Tafel slopes of the $Ni_{1-x}V_x$ LDHs catalysts from the LSV curves (**Fig. 5c)**. The measured Tafel slope values range from 48.1 to 84.79 $mVdec^{-1}$. The $Ni_{0.75}V_{0.25}$ LDH sample attains the smallest Tafel slope value of 48.1 $mVdec^{-1}$, revealing its superior OER kinetics and efficient electron transport [41,42]. The steady-state catalytic properties of the $Ni_{1-x}V_x$ LDH samples were measured using chronopotentiometry with multiple current steps from 10 mA cm^{-2} to 100 mA cm^{-2} (Supplementary Information **Fig. S15**); the $Ni_{0.75}V_{0.25}$ LDH catalyst also shows superior overpotential under continuously

elevated current density. **Figure 5d** presents the OER onset potential, overpotential at 10 mA cm^{-2}, and Tafel slope values obtained from the $Ni_{1-x}V_x$ LDH catalysts. The measured overpotential and Tafel slope curves are consistent with increasing V content, demonstrating that the $Ni_{0.75}V_{0.25}$ LDH has an electrocatalytically optimized Ni/V ratio, as theoretically anticipated in **Fig. 2c**. The best optimized $Ni_{0.75}V_{0.25}$ LDH catalyst for the OER activity is associated with synergy between the increased number of catalytically active sites, enhanced conductivity, and multiple oxidation states caused by V incorporation [19,22,39,43]. The consistent Tafel slope and onset potential results support that the optimized LDH sample has a superior intrinsic catalytic activity compared with the other LDH samples [41,42].

The OER catalytic activity of the $Ni_{1-x}V_x$ LDHs was further elucidated via geometric (electrochemically active surface area: ECSA) and electrical (Electrochemical Impedance Spectroscopy: EIS) analyses. First, the ECSA values of the catalysts were estimated by measuring the scan-rate-dependent CV curves in the non-faradaic voltage region. **Figure 6a** shows the CV curves of the $Ni_{0.75}V_{0.25}$ LDH catalyst measured at various scan rates. The ECSA of the catalyst is calculated using the following expression [44, 45].

$$\text{ECSA} = C_{DL}/C_S \tag{4}$$

where Cs is the specific capacitance in alkaline medium (0.040 mF cm^{-2} for the KOH electrolyte) and C_{DL} is the specific capacitance of the double-layer region. **Figure 6b** shows the non-faradaic capacitive current at 0.3 V as a function of scan rate (ν) for the NiV LDH samples. The slope of the capacitive current (Δj) measured at a non-faradaic voltage of 0.3 V versus scan rate is used to obtain the ECSA of the catalyst. As shown in **Figure 6c,** the largest ECSA value (460.75 cm^2) was obtained from the $Ni_{0.75}V_{0.25}$ LDH sample. As anticipated from the DFT calculations, the highest number of O active sites in the $Ni_{0.75}V_{0.25}$ LDH structure contributes to its superior ECSA. [39,46].

EIS measurements were carried out to further elucidate the electrocatalytic activity of $Ni_{1-x}V_x$ LDHs. **Figure 6d** shows the Nyquist curves of the LDHs samples, some of which exhibit a small semi-circle feature in the high-frequency region (**Fig. 6e**), which is associated with the charge-transfer resistance (R_{ct}). The Nyquist curves are modelled using the equivalent circuit diagram (inset in **Figure 6e),** in which R_s is the solution resistance and W_0 is the Warburg impedance. The main calculated parameters R_{ct} and R_s are shown in **Figure 6f**. The R_{ct} value of $Ni_{0.75}V_{0.25}$ LDH is 0.207 **Ω**, which is much smaller than those of the other catalysts. The increase in charge-transfer resistance of the Ni-V LDH samples with high V content ($x > 0.25$) could be due to the partial oxidation of V^{4+} to V^{5+} at the surface of the catalyst. The lowest charge-transfer resistance and fastest kinetics of the $Ni_{0.75}V_{0.25}$ LDH are in accordance with its superior OER activity.

The long-term stability of the $Ni_{1-x}V_x$ LDH catalysts was tested using a chronopotentiometry (CP) technique. **Figure 7a** shows the chronopotentiometry curves (without iR-correction) of the $Ni_{1-x}V_x$ LDH catalysts at 10 mA cm^{-2} under the same conditions used for the LSV measurements. All CP curves remain stable even for a very long time up to 100 h. **Figures 7b, c** show the LSV and CP curves of the best optimized $Ni_{0.75}V_{0.25}$ LDH sample before and after the long 100 h stability test. The overpotential values before and after the stability test at 10 mA cm^{-2} are 200 mV (before) and 206 mV (after), and remain almost unchanged even at a high current density of 400 $mAcm^{-2}$ (Supplementary Information **Fig. 16**). The electrocatalytic properties of the $Ni_{1-x}V_x$ LDHs are summarized in Supplementary Information **Table S2**. The best overall electrocatalytic performance is obtained from the $Ni_{0.75}V_{0.25}$ LDH catalyst.

To clarify the effect of long-term OER operation on the structural and chemical robustness of the best $Ni_{0.75}V_{0.25}$ LDH catalyst, we performed SEM, EDX, electrochemical impedance spectroscopy (EIS), and Raman spectroscopy measurements after the long-term

stability test. It is found that the catalyst retains its silk-like morphology (inset of **Fig. 7a**), revealing its excellent structural stability under vigorous oxygen bubbling. On the other hand, noticeable changes before and after the 100 h OER stability test are detected in the EDX (**Fig. 8a**), Raman spectra (**Fig. 8b) and EIS analysis (**Supplementary Information **Fig. S17**), and can be attributed to the transformation of the catalytically active phase during the long-term OER. After the long-term OER test, V deficiency is evident in the EDX analysis (**Fig. 8a**) and the existence of NiOOH is detected (475 cm^{-1} and 556 cm^{-1} in the Raman spectrum (**Fig. 8b**)) [47]. The transformation of $NiV(OH)_2$ to NiOOH at the surface causes V deficiency on the surface of the NiV LDH catalyst. Thus, it is reasonable to presume that the OER of the $Ni_{1-x}V_x$ LDHs is mediated through the formation of NiOOH at the surface of the catalyst.

4. Conclusions

In summary, we have comprehensively elucidated the electrocatalytic activities of $Ni_{1-x}V_x$ LDHs, both theoretically and experimentally, providing optimal rule-of-thumb design of dual-transition-metal layered double hydroxides for efficient oxygen evolution reaction. DFT calculations show that the enhanced conductivity due to the significant contribution of catalytically active oxygen (O) binding sites to the bands around the Fermi level facilitates the initiation of the OER process. The alteration of the local structural environment upon V doping (O charge attributed to V atoms) reduces the Gibbs free energy of O binding (ΔG_{O*}). The optimized $Ni_{0.75}V_{0.25}$ LDH has a lower hydrogen desorption energy and the most open O catalytically active sites. Ultra-low overpotentials of 200 and 292 mV at current densities of 10 and 400 mA cm^{-2}, respectively, are obtained for $Ni_{0.75}V_{0.25}$ LDH. This material also exhibits outstanding long-term durability for over 100 hours at 10 mA cm^{-2}, and a very low Tafel slope of 48.3 mV dec^{-1}. This work demonstrates a potential route for the design of state-of-the-art water oxidation catalysts for high performance and large-scale practical applications.

Declaration of Competing Interest

The authors declare no competing financial interests.

Acknowledgments

This work was supported by the Basic Science Research Program of the National Research Foundation of Korea (2021R1A4A5031805, 2021R1A2B5B01001796, 2018R1D1A1A09083859 and 2021R1A2B5B01002879) and the Creative Materials Discovery Program on Creative Multilevel Research Center (2018M3D1A1057844).

Appendix A. Supporting information

Supplementary data associated with this article can be found in the online version

References

[1] K. Fan, H. Chen, Y. Ji, H. Huang, P. M. Claesson, Q. Danie, B. Philippe, H. Rensmo, F. Li, Y.Luo, L. Sun, Nickel–vanadium monolayer double hydroxide for efficient electrochemical water oxidation, Nat. Commun. 7 (2016) 11981. doi: 10.1038/ncomms11981.

[2] Y. Lu, C. Yue, Y. Li, W. Bao, X. Guo, W. Yang, Z. Liu, P. Jiang, W. Yan, S. Liu, Y. Pan, Y. Liu, Atomically dispersed Ni on Mo_2C embedded in N, P co-doped carbon derived from polyoxometalate supramolecule for high-efficiency hydrogen evolution electrocatalysis Appl. Catal. B: Environ. 296 (2021) 120336. https://doi.org/10.1016/j.apcatb.2021.120336.

[3] W. Zhu, W. Chen, H. Yu, Y. Zeng, F. Ming, H. Liang, Z. Wang, NiCo/NiCo–OH and NiFe/NiFe–OH core shell nanostructures for water splitting electrocatalysis at large currents Appl. Catal. B: Environ. 278 (2020) 119326. https://doi.org/10.1016/j.apcatb.2020.119326.

[4] Y. Huang, X. Song, J. Deng, C. Zha, W. Huang, Y. Wu, Y. Li, Ultra-dispersed molybdenum phosphide and phosphosulfide nanoparticles on hierarchical carbonaceous scaffolds for

hydrogen evolution electrocatalysis, Appl. Catal. B: Environ. 245 (2019) 656–661. https://doi.org/10.1016/j.apcatb.2019.01.034.

[5] Z. Wang, P. Guo, S. Cao, H. Chen, S. Zhou, H. Liu, H. Wang, J. Zhang, S. Liu, S. Wei, D. Sun, X. Lu, Contemporaneous inverse manipulation of the valence configuration to preferred Co^{2+} and Ni^{3+} for enhanced overall water electrocatalysis, Appl. Catal. B: Environ. 284 (2021) 119725. https://doi.org/10.1016/j.apcatb.2020.119725.

[6] B. Wang, C. Tang, H.-F. Wang, X. Chen, R. Cao, Q. Zhang, A Nanosized CoNi Hydroxide@Hydroxysulfide Core–Shell Heterostructure for Enhanced Oxygen Evolution, Adv. Mater. 31 (2019) 1805658. https://doi.org/10.1002/adma.201805658.

[7] Z. Cui, G. Fu, Y. Li, J. B. Goodenough, Ni_3FeN-Supported Fe_3Pt Intermetallic Nanoalloy as a High-Performance Bifunctional Catalyst for Metal–Air Batteries, Angew. Chem., Int. Ed. 56 (2017) 9901-9905. https://doi.org/10.1002/anie.201705778.

[8] R. Francke, B. Schille, M. Roemelt, Homogeneously Catalyzed Electroreduction of Carbon Dioxide Methods, Mechanisms, and Catalysts, Chem. Rev. 118 (2018) 4631-4701. https://doi.org/10.1021/acs.chemrev.7b00459

[9] M. Shakeel, M. Arif, G. Yasin, B. Li, H. D. Khan, Layered by layered Ni-Mn-LDH/g-C3N4 nanohybrid for multi-purpose photo/electrocatalysis: Morphology controlled strategy for effective charge carriers separation, Appl. Catal. B: Environ. 242 (2019) 485–498. https://doi.org/10.1016/j.apcatb.2018.10.005.

[10] K. Zeng, D. Zhang, Recent progress in alkaline water electrolysis for hydrogen production and applications, Prog. Energy Combust. Sci. 36 (2010) 307-326. https://doi.org/10.1016/j.pecs.2009.11.002.

[11] Y. Li, Y. Sun, Y. Qin, W. Zhang, L. Wang, M. Luo, H. Yang, S. Guo, Recent Advances on Water-Splitting Electrocatalysis Mediated by Noble-Metal-Based Nanostructured Materials, Adv. Energy Mater. 10 (2020) 1903120. https://doi.org/10.1002/aenm.201903120.

[12] T. Reier, M. Oezaslan, P. Strasser, Electrocatalytic Oxygen Evolution Reaction (OER) on Ru, Ir, and Pt Catalysts: A Comparative Study of Nanoparticles and Bulk Materials, ACS Catal. 2 (2012) 1765-1772. https://doi.org/10.1021/cs3003098.

[13] Y. Qu, M. Yang, J. Chai, Z. Tang, M. Shao, C. T. Chi Tat Kwok, M. Yang, Z. Wang, D. Chua, S. Wang, Z. Lu, H. Pan, Facile Synthesis of Vanadium-Doped Ni_3S_2 Nanowire Arrays as Active Electrocatalyst for Hydrogen Evolution Reaction, ACS Appl. Mater. Interfaces 9 (2017) 5959-5967. https://doi.org/10.1021/acsami.6b13244.

[14] A. I. Inamdar, H. S. Chavan, B. Hou, C. H. Lee, S. U. Lee, S. N. Cha, H. Kim, H. Im. A Robust Nonprecious CuFe Composite as a Highly Efficient Bifunctional Catalyst for Overall Electrochemical Water Splitting, Small 16 (2020) 1905884. https://doi.org/10.1002/smll.201905884.

[15] J. L. Gunjakar, B. Hou, A. I. Inamdar, S. M. Pawar, A. T. A. Ahmed, H. S. Chavan, J. Kim, S.Cho, S. Lee, Y. Jo, S.-J. Hwang, T. G. Kim, S. N. Cha, H. Kim, H. Im, Two-Dimensional Layered Hydroxide Nanoporous Nanohybrids Pillared with Zero-Dimensional Polyoxovanadate Nanoclusters for Enhanced Water Oxidation Catalysis, Small 14 (2018) 1703481. https://doi.org/10.1002/smll.201703481.

[16] A. T. A. Ahmed, B. Hou, H. S. Chavan, Y. Jo, S. Cho, J. Kim, S. M. Pawar, S. N. Cha, A. I. Inamdar, H. Kim, H. Im. Self-Assembled Nanostructured $CuCo_2O_4$ for Electrochemical Energy Storage and the Oxygen Evolution Reaction via Morphology Engineering, Small 14 (2018) 1800742. https://doi.org/10.1002/smll.201800742.

[17] S. M. Pawar, B. S. Pawar, B. Hou, J. Kim, A. T. A. Ahmed, H. S. Chavan, Y. Jo, S. Cho, A. I. Inamdar, J. L. Gunjakar, H. Kim, S. N. Cha, H. Im, Self-assembled two-dimensional copper oxide nanosheet bundles as an efficient oxygen evolution reaction (OER) electrocatalyst for water splitting applications, J. Mater. Chem. A 5 (2017) 12747. https://doi.org/10.1039/C7TA02835K.

[18] H. Li, J. Wang, R. Qi, Y. Hu, J. Zhang, H. Zhao, J. Zhang, Y. Zhao, Enhanced Fe 3d delocalization and moderate spin polarization in Fe–Ni atomic pairs for bifunctional ORR and OER electrocatalysis, Appl. Catal. B: Environ. 285 (2021) 119778. https://doi.org/10.1016/j.apcatb.2020.119778.

[19] S. Fu, J. Song, C. Zhu, G.-L. Xu, K. Amine, C. Sun, X. Li, M. H. Engelhard, D. Du, Y. Lin, Ultrafine and highly disordered Ni_2Fe_1 nanofoams enabled highly efficient oxygen evolution reaction in alkaline electrolyte, Nano Energy 44 (2018) 319-326. https://doi.org/10.1016/j.nanoen.2017.12.010.

[20] C.-L. Zhang, J.-T. Liu, H. Li, L. Qin, F.-H. Cao, W. Zhang, The controlled synthesis of Fe3C/Co/N-doped hierarchically structured carbon nanotubes for enhanced electrocatalysis, Appl. Catal. B: Environ. 261 (2020) 118224. https://doi.org/10.1016/j.apcatb.2019.118224.

[21] L. Liu, Y. Ji, J. Nai, X. Niu, Y. Luo, L. Guo, S. Yang, Ultrathin amorphous cobalt–vanadium hydr(oxy)oxide catalysts for the oxygen evolution reaction, Energy Environ. Sci. 11 (2018) 1736-1741. https://doi.org/10.1039/C8EE00611C.

[22] P. Zhang, L. Li, D. Nordlund, H. Chen, L. Fan, B. Zhang, X. Sheng, Q. Daniel, L. Sun, Dendritic core-shell nickel-iron-copper metal/metal oxide electrode for efficient electrocatalytic water oxidation, Nat. Commun. 9 (2018) 381. DOI: 10.1038/s41467-017-02429-9.

[23] J. Zhang, H. Zhang, Y. Huang, Electron-rich NiFe layered double hydroxides via interface engineering for boosting electrocatalytic oxygen evolution, Appl. Catal. B: Environ. 297 (2021) 120453. https://doi.org/10.1016/j.apcatb.2021.120453.

[24] Y. Dou, L. Zhang, J. Xu, C.-T. He, X. Xu, Z. Sun, T. Liao, B. Nagy, P. Liu, S. X. Dou, Manipulating the Architecture of Atomically Thin Transition Metal (Hydr)oxides for Enhanced Oxygen Evolution Catalysis, ACS Nano 12 (2018) 1878-1886. https://doi.org/10.1021/acsnano.7b08691.

[25] M. S. Burke, S. Zou, L. J. Enman, J. E. Kellon, C. A. Gabor, E. Pledger, S. W. Boettcher, Revised Oxygen Evolution Reaction Activity Trends for First-Row Transition-Metal (Oxy)hydroxides in Alkaline Media, J. Phys. Chem. Lett. 6 (2015) 3737-3742. https://doi.org/10.1021/acs.jpclett.5b01650

[26] S. Zou, M. S. Burke, M. G. Kast, J. Fan, N. Danilovic, S. W. Boettcher, Fe (Oxy)hydroxide Oxygen Evolution Reaction Electrocatalysis: Intrinsic Activity and the Roles of Electrical Conductivity, Substrate, and Dissolution, Chem. Mater. 27 (2015) 8011-8020. https://doi.org/10.1021/acs.chemmater.5b03404.

[27] C. H. Lee, B. Jun, S. U. Lee, Metal-Free Oxygen Evolution and Oxygen Reduction Reaction Bifunctional Electrocatalyst in Alkaline Media: From Mechanisms to Structure–Catalytic Activity Relationship, ACS Sustainable Chem. Eng. 6 (2018) 4973-4980. https://doi.org/10.1021/acssuschemeng.7b04608.

[28] S. S. Shinde, C. H. Lee, J-Y. Yu, D-H. Kim, S. U. Lee, J-H. Lee, Hierarchically Designed 3D Holey C_2N Aerogels as Bifunctional Oxygen Electrodes for Flexible and Rechargeable Zn-Air Batteries, ACS Nano 12 (2018) 596-608. https://doi.org/10.1021/acsnano.7b07473

[29] S. S. Shinde, C. H. Lee, J.-Y. Jung, N. –K. Wagh, S.-H. Kim, D.-H. Kim, C. Lin, S. U. Lee, J.-H. Lee, Unveiling dual-linkage 3D hexaiminobenzene metal–organic frameworks towards long-lasting advanced reversible Zn–air batteries, Energy Environ. Sci. 12 (2019) 727-738. https://doi.org/10.1039/C8EE02679C.

[30] S. Anantharaj, P. E. Karthik, S. Kundu, Petal-like hierarchical array of ultrathin Ni(OH)2 nanosheets decorated with $Ni(OH)_2$ nanoburls: a highly efficient OER electrocatalyst, Catal. Sci. Technol. 7 (2017) 882-893. https://doi.org/10.1039/C6CY02282K.

[31] J. Jiang, F. Sun, S. Zhou, W. Hu, H. Zhang, J. Dong, Z. Jiang, J. Zhao, J. Li, W. Yan, M. Wang, Atomic-level insight into super-efficient electrocatalytic oxygen evolution on iron and vanadium co-doped nickel (oxy)hydroxide, Nat. Commun. 9 (2018) 2885. DOI: 10.1038/s41467-018-05341-y

[32] J. L. Gunjakar, A. I. Inamdar, B. Hou, S. Cha, S. M. Pawar, A. A. A. Talha, H. S. Chavan, J.Kim, S. Cho, S. Lee, Y. Jo, H. Kim, H. Im, Direct growth of 2D nickel hydroxide nanosheets intercalated with polyoxovanadate anions as a binder-free supercapacitor electrode, Nanoscale 10 (2018) 8953-8961. https://doi.org/10.1039/C7NR09626G

[33] D. G. Kellerman, T. G. Chukalkin, N. I. Medvedeva, M. V. Kuznetsov, N. A. Mukhina, A. S. Semenova, V. S. Gorshkov, Hydrogen reduction of vanadium in vanadium-doped $LiMnPO_4$ Mater. Chem. and physics 149-150 (2015) 209-215. https://doi.org/10.1016/j.matchemphys.2014.10.008.

[34] R. Baddour-Hadjean, M. B. Smirnov, K. S. Smirnov, V. Y. Kazimirov, J. Gallardo-Amores, U. Amador, M. E. Arroyo-de Dompablo, J. P. Pereira-Ramos, Lattice Dynamics of β-V_2O_5: Raman Spectroscopic Insight into the Atomistic Structure of a High-Pressure Vanadium Pentoxide Polymorph, Inorg. Chem. 51 (2012) 3194-3201. https://doi.org/10.1021/ic202651b

[35] B. Hou, P. Parker, G. P. Kissling, J. A. Jones, D. Cherns, D. J. Fermín, Structure and Band Edge Energy of Highly Luminescent $CdSe_{1-x}Te_x$ Alloyed Quantum Dots, J. Phys. Chem. C 117 (2013) 6814-6820. https://doi.org/10.1021/jp400208a

[36] H. S. Chavan, B. Hou, A. A. A. Talha, Y. Jo, S. Cho, J. Kim, S. M. Pawar, S. Cha, A. I. Inamdar, H. Im, H. Kim, Nanoflake $NiMoO_4$ based smart supercapacitor for intelligent power balance monitoring, Sol. Energy Mater. Sol. Cells 185 (2018) 166-173. https://doi.org/10.1016/j.solmat.2018.05.030.

[37] A. I. Inamdar, R. S. Kalubarme, J. Kim, Y. Jo, H. Woo, S. Cho, S. M. Pawar, C. J. Park, Y. W.Lee, J. I. Sohn, S. Cha, J. Kwak, H. Kim, H. Im, Nickel titanate lithium-ion battery anodes with high reversible capacity and high-rate long-cycle life performance, J. Mater. Chem. A 4 (2016) 4691-4699. https://doi.org/10.1039/C5TA10528E

[38] Z. Xue, X. Li, Q. Liu, M. Cai, K. Liu, M. Liu, Z. Ke, X. Liu, G. Li, Interfacial Electronic Structure Modulation of NiTe Nanoarrays with NiS Nanodots Facilitates Electrocatalytic Oxygen Evolution, Adv. Mater. 31 (2019) 1900430. https://doi.org/10.1002/adma.201900430.

[39] M. Gao, W. Sheng, Z. Zhuang, Q. Fang, S. Gu, J. Jiang, Y. Yan, Efficient Water Oxidation Using Nanostructured α-Nickel-Hydroxide as an Electrocatalyst, J. Am. Chem., Soc. 136 (2014), 7077-7084. https://doi.org/10.1021/ja502128j.

[40] J. S. Kim, B. Kim, H. Kim, K. Kang, Recent Progress on Multimetal Oxide Catalysts for the Oxygen Evolution Reaction, Adv. Energy Mater.8 (2018) 1702774. https://doi.org/10.1002/aenm.201702774.

[41] M. Huynh, C. Shi, S. J. L. Billinge, D. G. Nocera, Nature of Activated Manganese Oxide for Oxygen Evolution, J. Am. Chem. Soc. 137 (2015) 14887-14904. https://doi.org/10.1021/jacs.5b06382.

[42] R. D. L. Smith, M. S. Prévot, R. D. Fagan, S. Trudel, C. P. Berlinguette, Water Oxidation Catalysis: Electrocatalytic Response to Metal Stoichiometry in Amorphous Metal Oxide Films Containing Iron, Cobalt, and Nickel, J. Am. Chem. Soc. 135 (2013) 11580-11586. https://doi.org/10.1021/ja403102j.

[43] L. Yu, H. Zhou, J. Sun, F. Qin, F. Yu, J. Bao, Y. Yu, S. Chen, Z. Ren, Cu nanowires shelled with NiFe layered double hydroxide nanosheets as bifunctional electrocatalysts for overall water splitting, Energy Environ. Sci. 10 (2017) 1820-1827. https://doi.org/10.1039/C7EE01571B.

[44] V. Kannan, A. I. Inamdar, S. M. Pawar, H. S. Kim, H. C. Park, H. Kim, H. Im, Y. S. Chae, Facile Route to NiO Nanostructured Electrode Grown by Oblique Angle Deposition Technique for Supercapacitors, ACS Appl. Mater. Interfaces 8 (2016) 17220-17225. https://doi.org/10.1021/acsami.6b03714.

[45] A. I. Inamdar, H. S. Chavan, S. M. Pawar, H. Kim and H. Im, NiFeCo oxide as an efficient and sustainable catalyst for the oxygen evolution reaction, Int J Energy Res. 44 (2020) 1789-1797. https://doi.org/10.1002/er.5026.

[46] G. Zhang, Y. Meng, B. Xie, Z. Ni, H. Lu, S. Xia, Precise location and regulation of active sites for highly efficient photocatalytic synthesis of ammonia by facet-dependent BiVO4 single

crystals, Appl. Catal. B: Environ. 296 (2021) 120379. https://doi.org/10.1016/j.apcatb.2021.120379.

[47] J. Zhou, L. Yu, Q. Zhou, C. Huang, Y. Zhang, B. Yu, Y. Yu, Ultrafast fabrication of porous transition metal foams for efficient electrocatalytic water splitting, Appl. Catal. B: Environ. l 288 (2021) 120002. https://doi.org/10.1016/j.apcatb.2021.120002.

Figures

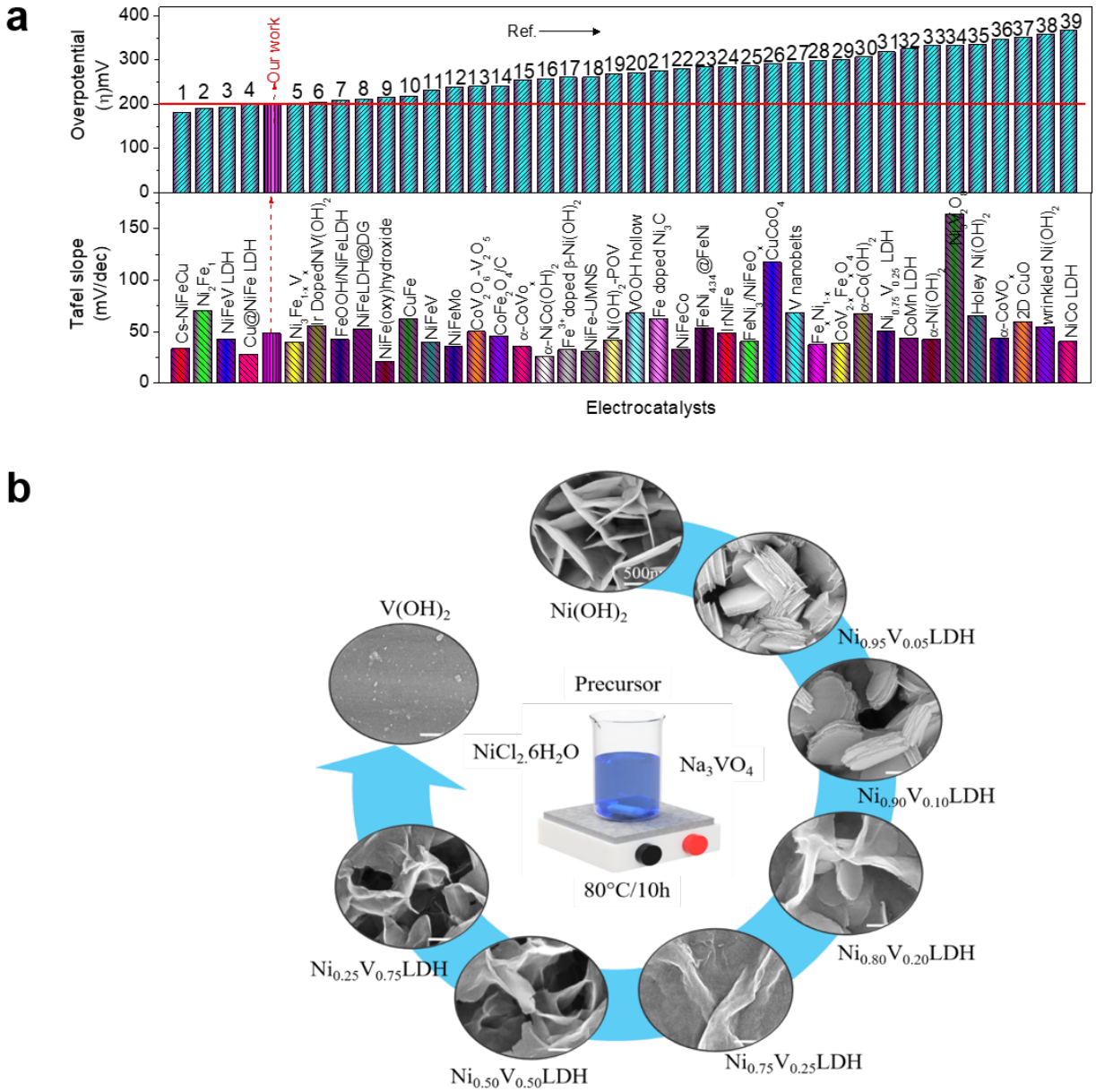

Fig. 1. (a) Literature survey results and comparison of reported overpotentials at 10 mA cm^{-2} and Tafel slopes for various electrocatalysts, supplimentary references[1-39], including our sample, (b) Schematic showing the growth processes of the Ni_xV_{1-x} layered double hydroxides (LDHs) using chemical bath deposition (CBD), along with their morphologies.

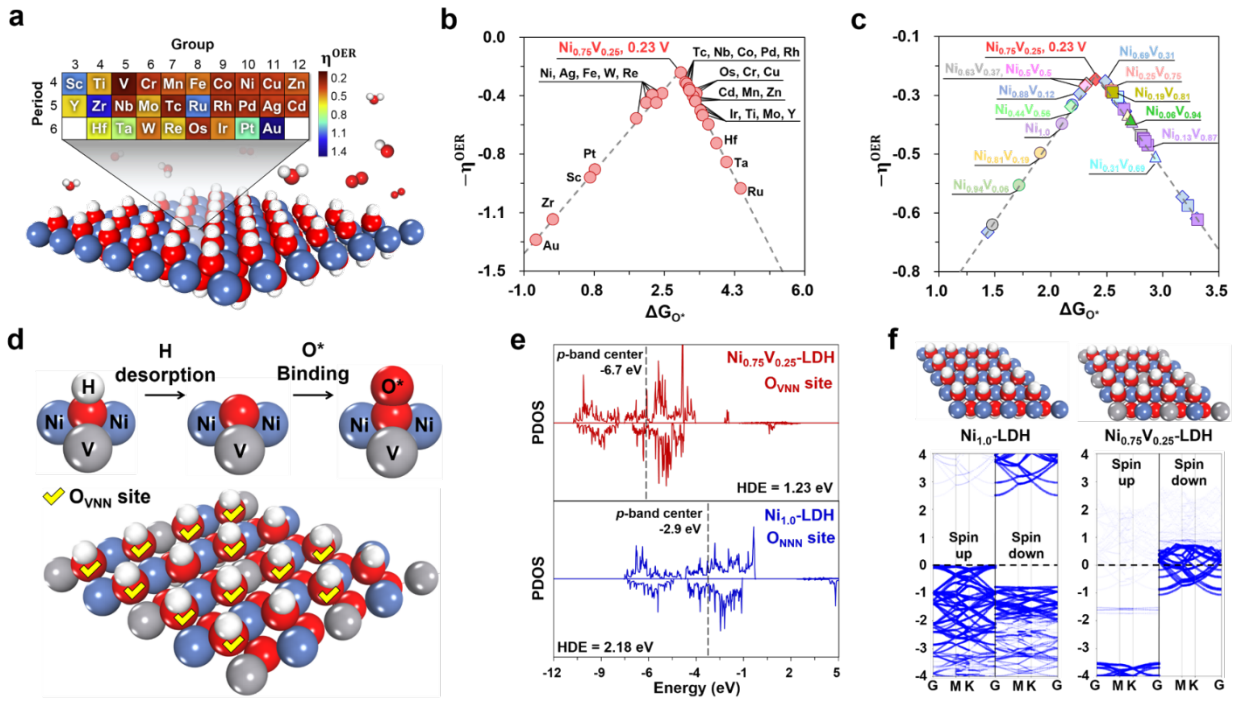

Fig. 2. Theoretical evaluation of the oxygen evolution reaction (OER) catalytic activities of Ni-transition metal (TM) layered double hydroxide (LDH) structures. (a) Schematic of the OER activity screening of the Ni-TM LDH structures. (b) OER volcano plots of (b) the $Ni_{0.75}TM_{0.25}$ LDH and (c) the $Ni_{1-x}V_x$ LDH ($0 \leq x \leq 1$) structures. (d) Schematic of the OER active site and reaction mechanism of the $Ni_{0.75}V_{0.25}$ LDH structure. (e) *p*-band centers of the oxygen (O) active sites (O_{VNN} and O_{NNN}, where V = vanadium and N = nickel) analyzed using the partial density of states (PDOS) method on the $Ni_{0.75}V_{0.25}$ LDH and $Ni_{1.0}$ LDH structures. (f) Elemental decomposition band structures of the O active sites in the $Ni_{1.0}$ LDH and $Ni_{0.75}V_{0.25}$ LDH structures. The Fermi levels are indicated by black dashed lines. Blue-grey, grey, red, and white colors represent Ni, V, O, and hydrogen (H), respectively.

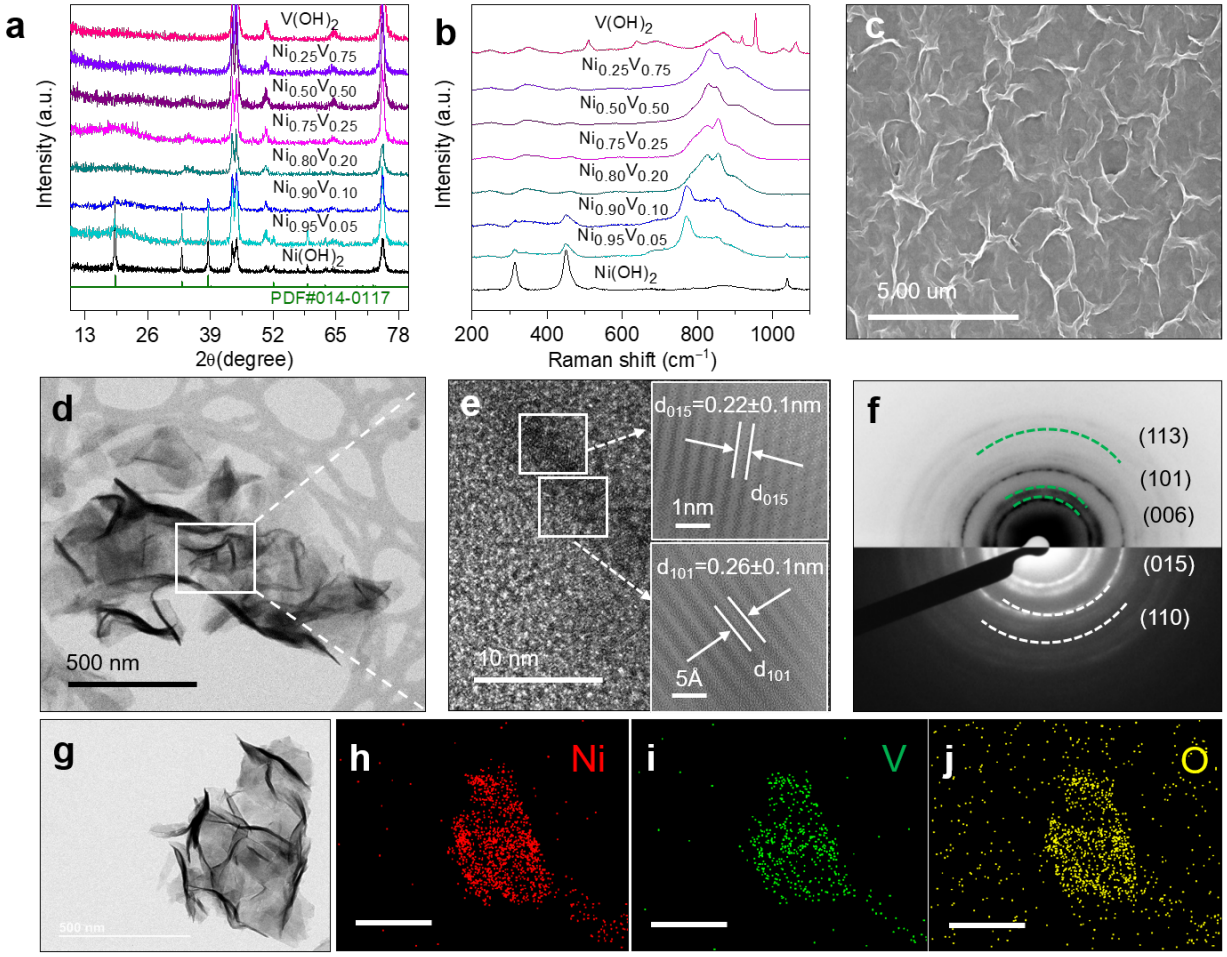

Fig. 3 (a) X-ray diffraction (XRD) pattern of the $Ni_{1-x}V_x$ layered double hydroxide (LDH) electrodes along with the standard JCPDS (14-0117) data (* indicates the signal from the stainless-steel substrate). (b) Raman spectra of the $Ni_{1-x}V_x$ LDH electrodes. (c) High magnification scanning electron microscopy (SEM) image of the silk-like structure of the $Ni_{0.75}V_{0.25}$ LDH. (d) Transmission electron microscopy (TEM) image of $Ni_{0.75}V_{0.25}$ LDH. (e) High-resolution TEM images of the selected area in (d) showing lattice fringes with distances of 0.22 and 0.26 nm in the inset. (f) SAED pattern showing the diffuse ring feature of the $Ni_{0.75}V_{0.25}$ LDH. (g–j) High-angle annular dark field-scanning transmission electron microscopy (HAADF-STEM) image and EDX elemental mapping of the $Ni_{0.75}V_{0.25}$ LDH silk-like structure under TEM mode revealing the homogeneous distribution of Ni (red), V (green), and O (yellow) in the sample.

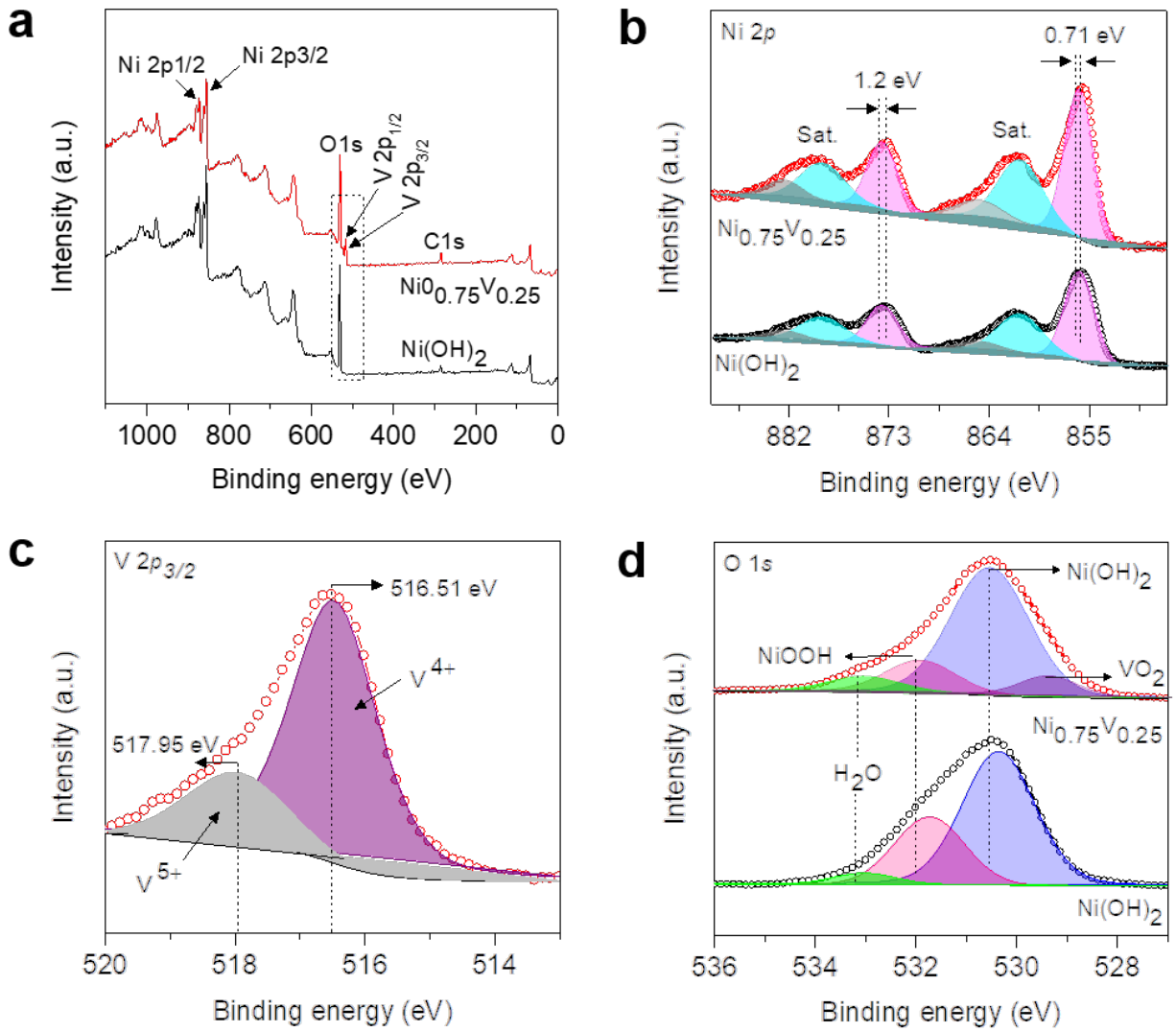

Fig. 4 (a) Overlapping X-ray photoelectron spectroscopy (XPS) survey spectra of the nickel hydroxide ($Ni(OH)_2$) and $Ni_{0.75}V_{0.25}$ layered double hydroxide (LDH) electrodes revealing the existence of Ni, V, and O as the constituent elements. (b) Overlapping Ni 2p peaks of $Ni(OH)_2$ and $Ni_{0.75}V_{0.25}$ LDH, (c) deconvoluted V $2p_{3/2}$ peak of $Ni_{0.75}V_{0.25}$ LDH, and (d) O 1s peaks of $Ni(OH)_2$ and $Ni_{0.75}V_{0.25}$ LDHs. The circles and lines represent the experimental data and fitted curves, respectively.

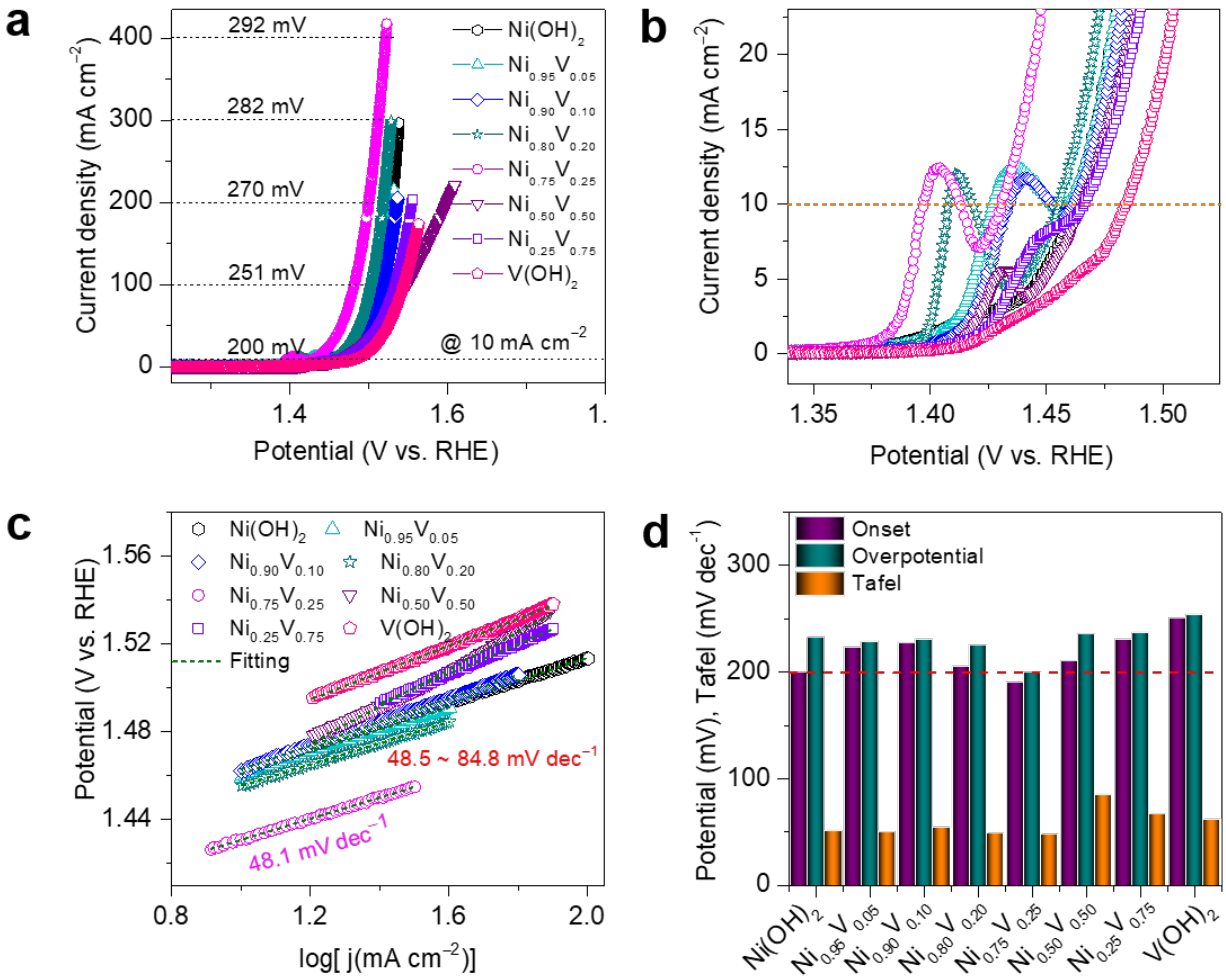

Fig. 5 Electrochemical characterization of the $Ni_{1-x}V_x$ layered double hydroxide (LDH) electrodes. (a) Polarization curves of the LDH catalysts and (**b**) the enlarged region of the curves in (a). The LSV curves are iR-corrected. (c) Tafel plots. (d) Summary of the measured onset potential, overpotential at 10 mA cm^{-2}, and Tafel slope values.

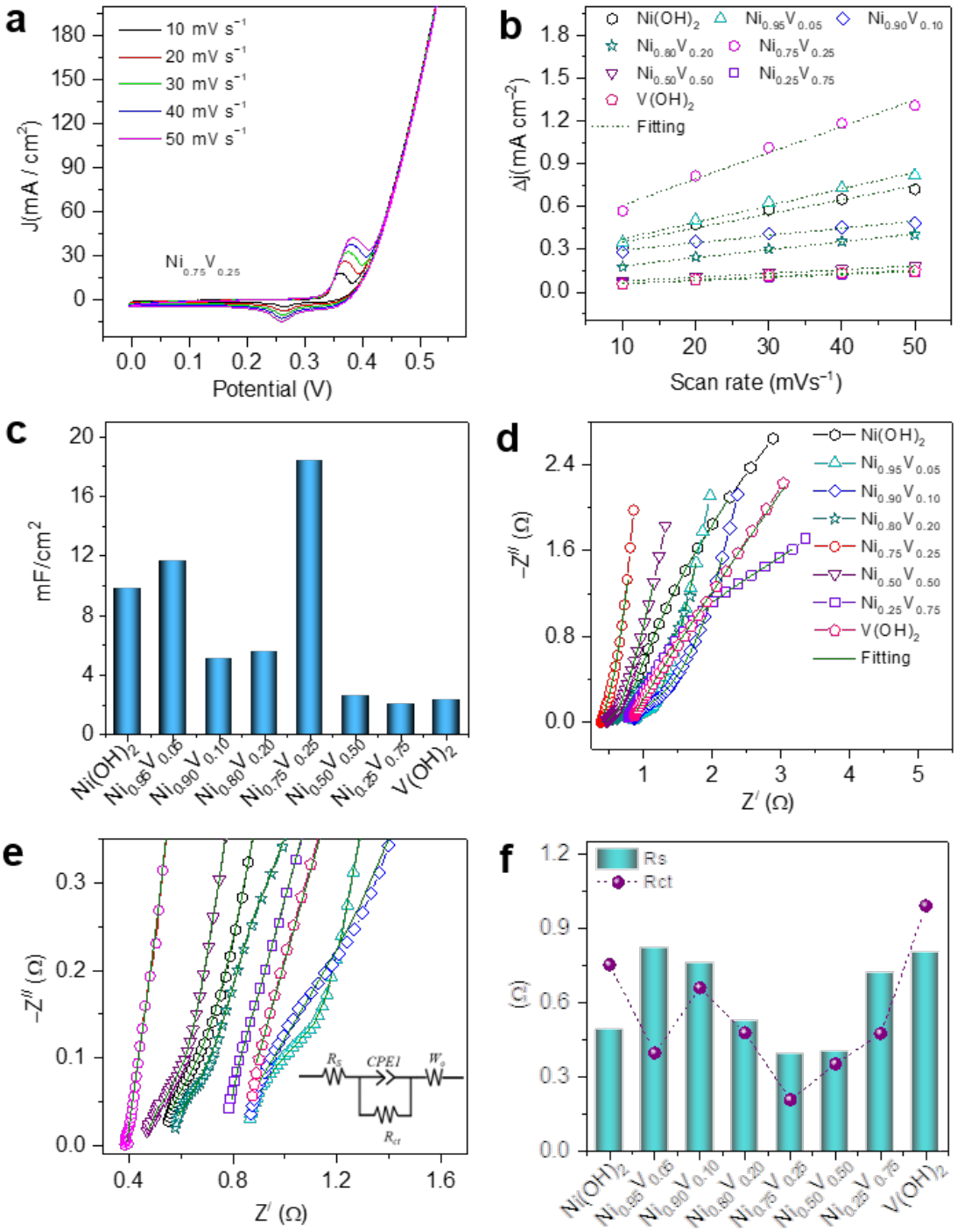

Fig. 6 (a) Typical cyclic voltammetry (CV) curves of $Ni_{0.75}V_{0.25}$ LDH recorded at different scan rates of 10, 20, 30, 40, and 50 mVs^{-1}. (b) Plot of current density (Δj) versus scan rate (mVs^{-1}), from which the electrochemically active surface areas (ECSAs) were determined. (c) Calculated ECSA values. (d) Nyquist plots of the catalysts measured at zero biasing. (e) enlarged view of the Nyquist plots (f) Summary of the extracted EIS parameters.

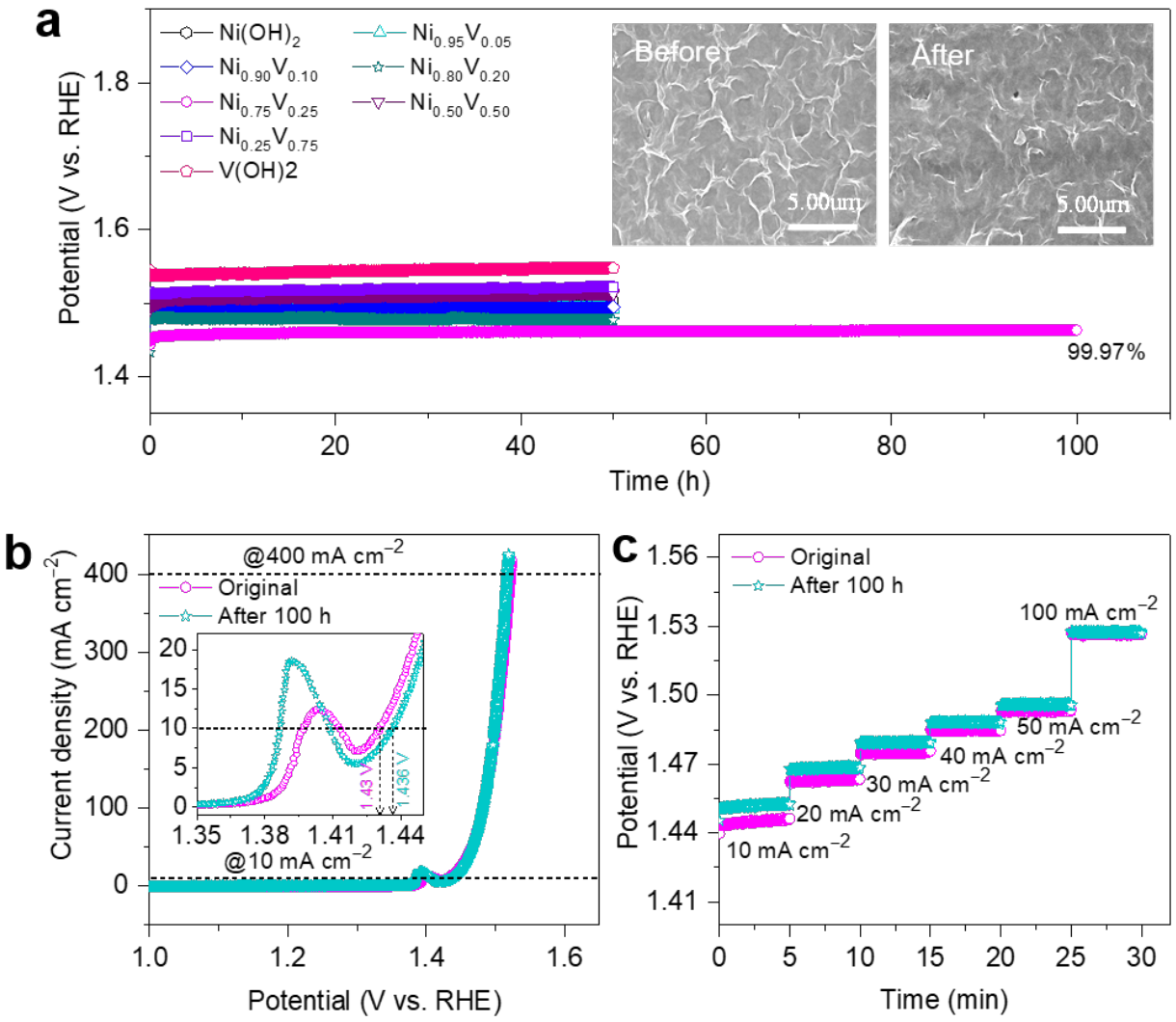

Fig. 7 (a) Chronopotentiometric curves obtained from $Ni_{1-x}V_x$ layered double hydroxide (LDH) catalysts in 1 M potassium hydroxide (KOH) at a constant current density of 10 mA cm^{-2}. The inset shows scanning electron microscopy (SEM) images of the optimized $Ni_{0.75}V_{0.25}$ LDH catalyst before and after long-term stability testing, revealing its mechanical robustness during the oxygen evolution reaction (OER) electrocatalysis. (b) Linear sweep voltammetry (LSV) curves of the $Ni_{0.75}V_{0.25}$ LDH electrode before and after 100 h stability testing. (c) Multi-current process obtained for $Ni_{0.75}V_{0.25}$ LDH before and after 100 h stability testing.

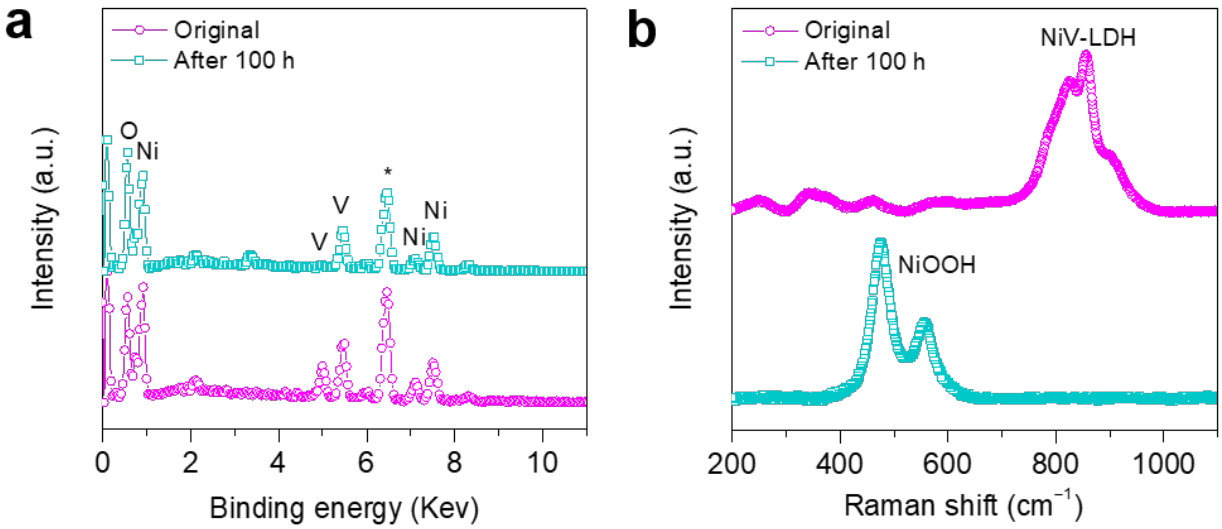

Fig. 8. (a) Energy-dispersive X-ray spectroscopy (EDX) data obtained before and after 100 h stability testing for the best $Ni_{0.75}V_{0.25}$ layered double hydroxide (LDH) sample. (b) Raman spectra of $Ni_{0.75}V_{0.25}$ LDH before and after the long-term stability test.